School of Industrial and Information Engineering
Master of Science in Automation and Control Engineering

POLITECNICO
MILANO 1863

ADMITTANCE CONTROL OF A HANDHELD MICROSURGICAL INSTRUMENT

Supervisor: Prof. Luca BASCETTA
Prof. Cameron N. RIVIERE

MSc Thesis of:
Giulio RUSSO
Matr. 892271

Academic Year 2018 - 2019

Ai miei genitori

Sommario

Nelle procedure di dissezione in neurochirurgia, vengono eseguite operazioni ad elevato grado di precisione ed accuratezza in condizioni di scarsa visibilita'. Il sanguinamento causato dall'errato posizionamento degli strumenti rispetto ai vasi sanguigni e' una delle complicanze piu' comuni (10.2%) [1].
La protezione dei vasi sanguigni e la prevenzione del sanguinamento rimangono di primaria importanza: numerosi sistemi robotici sono stati sviluppati per assistere i chirurghi negli interventi neurochirurgici.
I bracci robotici sono di difficile utilizzo a causa delle grandi dimensioni, dei costi elevati, dell'incapacita' di adattarsi alle mutevoli condizioni e dell'aumento rilevante del tempo di esecuzione delle operazioni.
Tutti questi problemi possono essere risolti utilizzando uno strumento robotico impugnabile, utilizzato come un bisturi: facilmente manovrabile, garantisce una coordinazione intuitiva dei movimenti e la compensazione del tremore.

Il seguente progetto riguarda l'utilizzo di uno strumento impugnabile robotizzato (Micron) progettato dal *Robotics Institute* della *Carnegie Mellon University*: il suo obiettivo principale e' garantire la compensazione del tremore e la riduzione delle forze esercitate sui tessuti durante gli interventi chirurgici.

Un controllo di ammettenza e' stato progettato e implementato con lo scopo di ridurre le forze di interazione tra end-effector e i tessuti. Inoltre, un test sperimentale e' stato utilizzato per simulare un ambiente chirurgico e l'interazione tra Micron e i tessuti: sono state valutate efficacia e affidabilita' del controllo implementato.

I risultati evidenziano come il progetto presentato aiuti a ridurre i danni ai tessuti, supportando i chirurghi nell'eseguire le operazioni, evitando, in modo sicuro, i vasi sanguigni durante le procedure neurochirurgiche.

Abstract

In neurosurgical procedures for blunt dissection, minute and accurate operations in poor visibility conditions have to be performed. Bleeding caused by tools misplacement with respect to the vessels is one of the most common complications (10.2%) [1].
Preservation of large vessels and bleeding avoidance remain of primary importance: numerous robotic systems have been developed to assist surgeons in microneurosurgical interventions. Robotic arms are pointless due to drawbacks such as large size and high cost, limited functions, inability to adapt to changing conditions and increased operative time.
All these issues can be overcome by using an active handheld instrument, used like a scalpel and which guarantees dexterous manipulation capability, hand-tool coordination, tremor compensation and ability to adapt.

The present work investigates the use of a robotic handheld tool (Micron) designed by the *Robotics Institute* of the *Carnegie Mellon University*: designed to perform surgery while compensating tremor and reducing the contact forces.
An admittance system has been designed to achieve a reliable and effective control strategy, which reduces the interaction forces between the end effector and the tissues.
An experimental set-up has been developed in order to simulate Micron-tissues interaction in a surgical environment: tests have been performed to examine the efficiency and reliability of the admittance control.

The results suggested that the presented work is helpful in reducing the tissues damages, supporting surgeons in performing safe vessels avoidance in neurosurgical procedures.

Contents

List of Figures

Chapter 1

Clinical background

1.1 Introduction

In this chapter the clinical background and the neurosurgical procedures that benefit more from the designed instrument are introduced.

1.2 Petroclivial Meningioma

During neurosurgical procedures, surgeons have to perform minute and accurate operations with poor visibility [2].
One of the most common complication in cranial surgeries (5.4%) [3] is bleeding. Misplacement of surgical tools with respect to vessels can cause several deficits, such edema, seizures, postoperative haemorrhage, and cerebral ischemia, compromising post-operative recovery [3].
Hence, preservation of large vessels and bleeding avoidance are of primary importance to reduce patience morbidity and mortality [4]. In particolar, postoperative rates of cerebral infarction and cranial nerve deficits are high and dramatically reduce quality of life in patients [4].

Meningioma resections are the procedures that could benefit more from the instrument designed in this work.
Different kinds of meningiomas can be distinguished depending on their location: the most relevant for this project is the Petroclival meningioma.

Petroclivial meningioma resection is known as one of the most technically challenging neurosurgical procedures: it is a tumor that arise from the apical petrous bone and/or clivus with extension to the sphenoid bones or cavernous sinus. The proximity and adhesion of the tumor to cranial

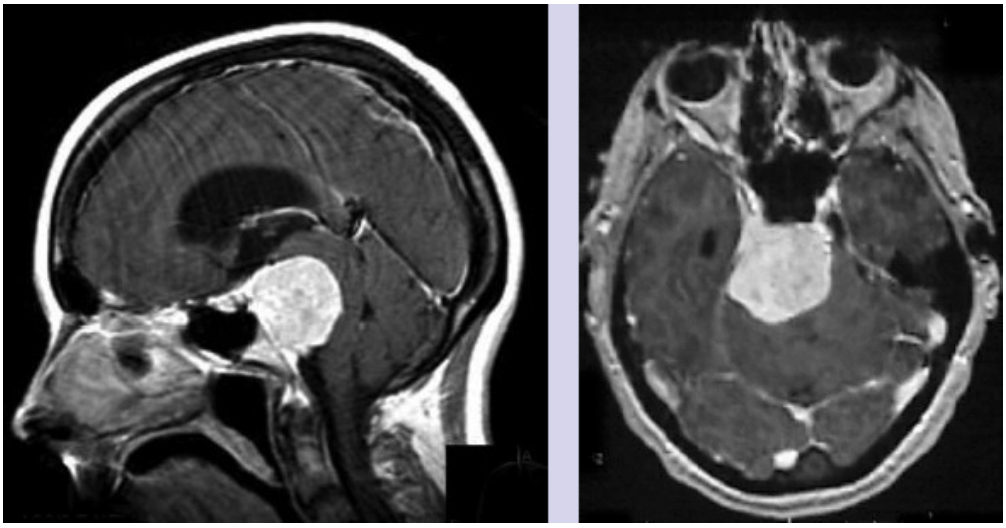

Figure 1.1: *Petroclival meningioma.*

nerves and blood vessels increase the risk of postoperative morbidity and mortality [5].

Meningiomas account for 20 to 25% of all intracranial tumors and 10% are seen in the posterior fossa. Among posterior fossa meningiomas, those arising from the petroclival region account for 5 to 11% of meningiomas and thus 0.15% of all intracranial tumors.

The most common morbidities, reported in [5], were cranial nerve deficits (34.4% with a range from 20 to 79%) with facial nerve injury accounting for 19%, followed by motor deficits (14%), infection rates (1.6%), hemorrhage (1.2%), and hydrocephalus (1%). Death within 1 year of surgery was reported for 1.4% of patients. More than 75% of patients return to independence at 1 year.

Different surgical approaches for treatment of petroclival meningiomas exist: the location, size, extension of the meningioma and patience age affect the choice of the surgical approach.

Chapter 2

State of art

2.1 Introduction

In this chapter an overview of the interaction control strategy implemented in neurosurgery tools is reported: the most recent instrumentations are introduced together with their force control strategies.

2.2 Neurosurgery keyhole

Robot assistance is of relevant importance in surgery: the use of robots allows surgeons to work with precision by suppressing involuntary movements, permits the use of smaller instruments and incisions, reducing the healing time.

First surgery-robots for neurosurgery come from experiences in the industrial sector, they performed simple stereotactic tasks: patient positioning [6], trajectory planning [7], and tumor resection [8].
Robots able to perform operative tasks were then proposed in [9, 10, 11, 12]: they concern single dimensional incursions into the brain, assisted by computed tomography system.

In the last years, the *cooperative robot control* is popular: a surgeon guides the end of a robot arm using an attached grip that sense the force applied by the hand. NeuroMate is one of the first image-guided robotic system used for stereotactic procedures in neurosurgery [9, 13, 14].

Furthermore, the *master-slave teleoperation* [15] is the most famous and used approach to surgical robots for microsurgery: motion scaling and

Figure 2.1: *NeuroMate, an example of cooperative robot used for neurosurgeries.*

filtering of tremor are used to achieve improved accuracy.

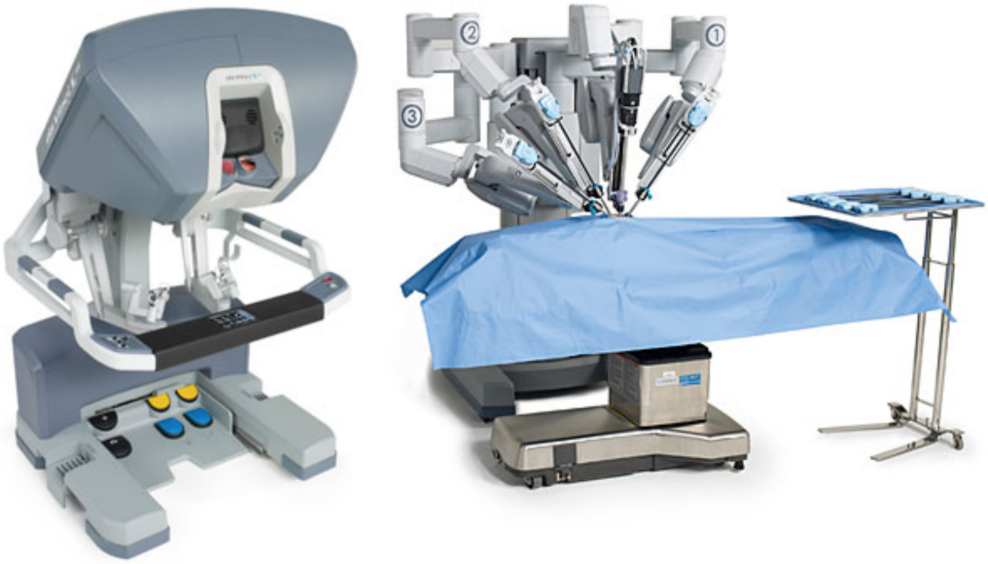

Figure 2.2: *Da vinci: master-slave robotic system for neurosurgeries. The master is on the left side of the image, while the slave is represented on the other side.*

2.3 Handheld tools

A third solution which deals with *handheld robotic system* has been proposed: intuitive operation, safety and economy [16] are the main advantages compared to master-slave and cooperative systems.

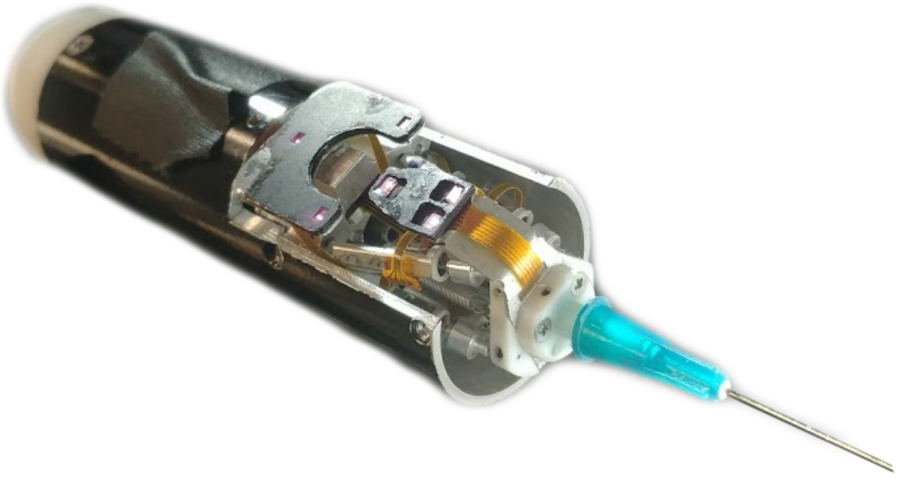

Figure 2.3: *Micron, an example of handheld robot system used for neurosurgeries.*

The main goal is to allow the surgeon to reduce larger unintended movements of the human hand, resulting in reduced morbidity and mortality rate for patients [17]. This approach offers the same intuitive feel as a conventional unaided tool, coordination hand-robot and intuitive operation are of mainly importance for surgeons acceptance.
Then, following the Riviere approach [18], the idea is to retain the advantages possessed by the surgeon, improving accuracy and precision of the tool.
Furthermore, handheld tools guarantee a lower workspace intrusion with respect to the previous approaches [19]: due to the amount of equipment already in use in the operating room, it represents a good point.
The handheld tools are used in various medical fields: orthopedics, gynecology, general microsurgeries and ophthalmology, etc. But even though all these instruments are used in extremely different procedures, they are built in the same way.

2.4 Method for force sensing

The common direct methods for force sensing [20] concern strain gauges, piezoelectric sensors optical sensors.

Piezoelectric sensors are commonly used in surgery: a voltage variation from the material (piezoelectric materials) is detected when mechanical stress applied. They are famous for large measurements range, high bandwidths, small sizes. However due to temperature changes and charge leakages, the signal drifts, becoming inappropriate for static force measurements.

Strain gauges are the most used method in surgery for their good performance with small size, fine sensitivity, easy multi-axis measurements and high strength during force sensing. However, drift and hysteresis are very challenging due to temperature variation and electromagnetic noise.

Optical sensors, based on the varying intensity or phase from a light signal, is able to acquire with multiple degrees of freedom with high sensitivity, reproducibility and no hysteresis: Fiber Bragg Grating is popular even if it is limited by cable deformation and calibration.

2.5 Interaction control strategies

In robotic application, position control is not enough due to unknown interaction between the robot and the environment. In many cases the integration of force information to the control loop is necessary to allow assembly, object handling, examination, haptic exploration tasks, etc. Force based control algorithms, provided with force sensors, give a natural extension to the medical robots: human-machine interaction, realistic sensory feedback, safety and dependability in interaction are few of the necessary feature during surgery procedures.
During manipulator-environment interaction, the robot has to achieve desired dynamic behaviors: providing the needed force to overcome the environment's resistance, or to comply with it.

There exist two main idea of interaction control strategy [21]:

- In *indirect force control*, the force control is achieved via motion control, without ensuring a force feedback loop: the position error

is related to the contact force through impedance or mechanical stiffness.

- In *direct force control*, it's possible to achieve a desired force value, ensuring a force control loop closed around the inner motion control loop.

Admittance control and *impedance control* belong to the first category: the position error is related to the contact force through a mechanical admittance or impedance.
If a detailed model of the environment is available, the *hybrid positon/force control*, second category, allows to control the position along the unconstrained task directions and force along the constrained task directions.
When a detailed model of the environment is not available, a *parallel control* can be used: an outer force control loop dominates a inner position control loop, in order to ensure a force tracking along the constrained task directions.

In neurosurgery procedure, obviously it's really hard to model the environment due to a great diversity of tissues. Furthermore, surgeons don't need to track a force reference but need to avoid the force thresholds exceeding. To achieve these goals, impedance and admittance control are of greater interest.

The impedance control is better suited for small forces and slow motions, it needs a precise dynamic manipulator model. The admittance control is better suited for high accuracy positioning requiring stiff joint position. The robot dynamic model is not required.
While these kinds of control are of main importance and already used for cooperative robot control [22] and for master-slave teleoperation [23], they are new for handheld tools in surgery.

Recently, handheld and ungrounded force-feedback systems have been developed in order to provide force-feedback active constraint to warn the surgeon. However, the control strategy is not reducing the applied forces itself [24].
The implementation of a force control in a one degree of freedom handheld manipulator was described by Latt et al. in [25].
Besides, the first implementation of force control in a fully handheld manipulator with multiple degrees of freedom was developed by Wells et al. in [26]: it concerns a hybrid position/force control for a handheld tool for surgery called Micron, used to limit the applied forces to reduce

tissues' damages. Reduction around 40% were achieved for the forces for vitreoretinal microsurgery.

2.6 Objective of the thesis

As an alternative approach with a clearer physical interpretation and more suitable for neurosurgery procedures, this work presents an admittance control approach: the objective of this thesis is aimed at reducing applied forces during surgical procedures with the handheld robot developed at the *Surgical Mechatronics Laboratory* of the *Carnegie Mellon University*: Micron.

Specifically:

- In *Chapter 3*, the architecture and control of Micron are described.
- In *Chapter 4*, the theory of classic interaction problems are explained, focusing on admittance control.
- In *Chapter 5*, a customize admittance control for Micron is designed and implemented.
- In *Chapter 6*, the new developed admittance control is tested and results are showed.

Chapter 3

Micron

3.1 Introduction

In this chapter the architecture and control of the concerned handheld tool for neurosurgery are explained.

Micron is an actively handheld surgical robot [fig. 3.1]. It allows surgeons to directly maneuver surgical tools, remaining in gross control of them at all times, while selectively filtering out erroneous motion such as hand tremor. The design of Micron allows surgeons to attain the natural feel of manual operation and direct tactile feedback from the tool attached.

Figure 3.1: *Micron, an handheld tool for neurosurgery.*

3.2 Architecture

The instrument is composed by an handle and an end-effector: it is 28.5mm in diameter and 126mm long, excluding the end-effector (a needle). The total mass is 70.0g. Below the main components of the manipulator are explained:

- a Gough-Stewart platform is attached between the end effector (moving platform) and the handle (handle platform): it's actuated by 6 linear piezoelectric actuators (SQL-RV-1.8 SQUIGGLE motor, New Scale Technologies, Inc., Victor, NY) and allows maneuverability in the desired cylindrical workspace (4.00 x 4.00 mm)

Figure 3.2: *Gough Stewart Platform compared with a quarter of Dollar*

- the end effector, connected on the moving platform, is a surgery tool: in this project it has been used a needle (36 mm long). A FBG force sensor is embedded with the end effector tool, allowing force feedback with 0.25 mN resolution (section 3.5): the sensor has 2 degree of freedom, allowing force measurement perpendicular to the end-effector.

- Since the Fiber Bragg Grating force sensor has just two degrees of freedom, to emulate a force sensor with three degrees of freedom, the sensor was augmented with a load cell mounted underneath the workpiece: the load cell data were fused with the onboard sensing to obtain the force parallel to the long axis of the instrument.

- on the manipulator, six frequency modulated LEDs are placed in order to enable optical tracking of the position and orientation of

both the tool tip and the handle: three of them are mounted on the handle and the remaining three on the moving platform. The Apparatus to Sense Accuracy of Position (ASAP), provided with two Position-Sensitive-Detector (PSD) cameras, senses the differently modulated signals using frequency domain multiplexing and provide an analog position measurement of the centroid of each light source [27]. Then, the poses of the tool tip and the handle are recovered from the triangulation in three dimensions of each triad of LEDs: it's possible to know the position of the manipulator within a $27cm^3$ workspace with a frequency of $1000Hz$ [27].

3.3 Tremor characteristics

With the aim of designing a filter able to remove the erroneous and undesired movements, tremor characteristic have been analyzed in [28]. In this work, tremor means any involuntary hand motion that creates position error.
In figure 3.3, the typical motions when a subject tries to hold a tip stationary are showed:

- *High frequency quasi-periodic motion.*
- *Drift* or *wander* is a slow trend;
- *Jerk* is a sporadic fast jump;

It is necessary to suppress all these motions to achieve useful stabilization.

Furthermore, figure 3.4 is the acceleration and position spectrum of the hand motion: it's obvious that the accelaration has a peak around $10Hz$, it suits the medical definition of tremor. While, the bandwidth of human eye-hand coordination generally lies between 0.5 and $2Hz$: the eye-hand feedback becomes effective below this critical frequency.

Clearly the human motion is a non linear system, really complex to modelize. But in this project, the human motion has been reduced to a linear system: even if this approximation neglects many details, it has been successfully used.

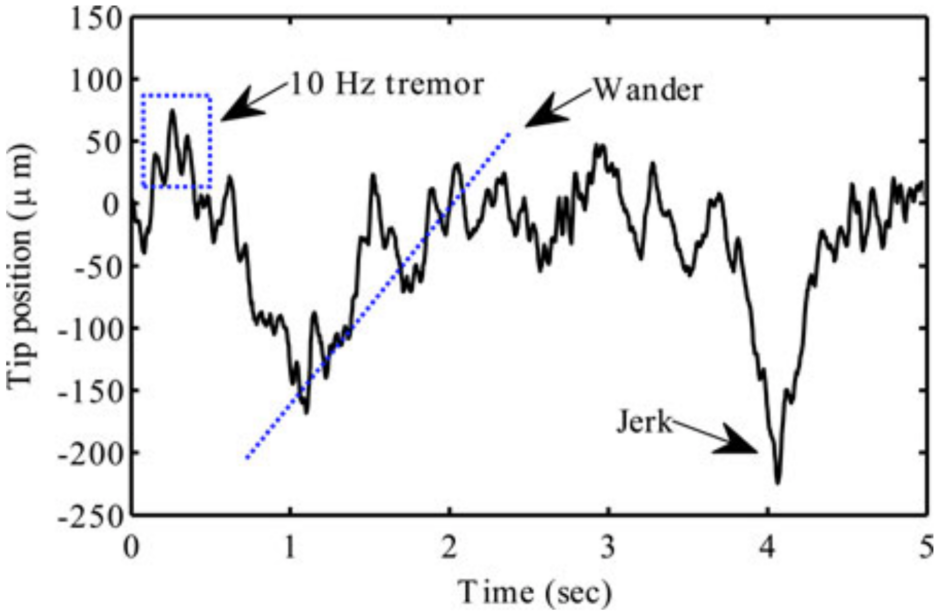

Figure 3.3: *Tremor signal and identified features.*

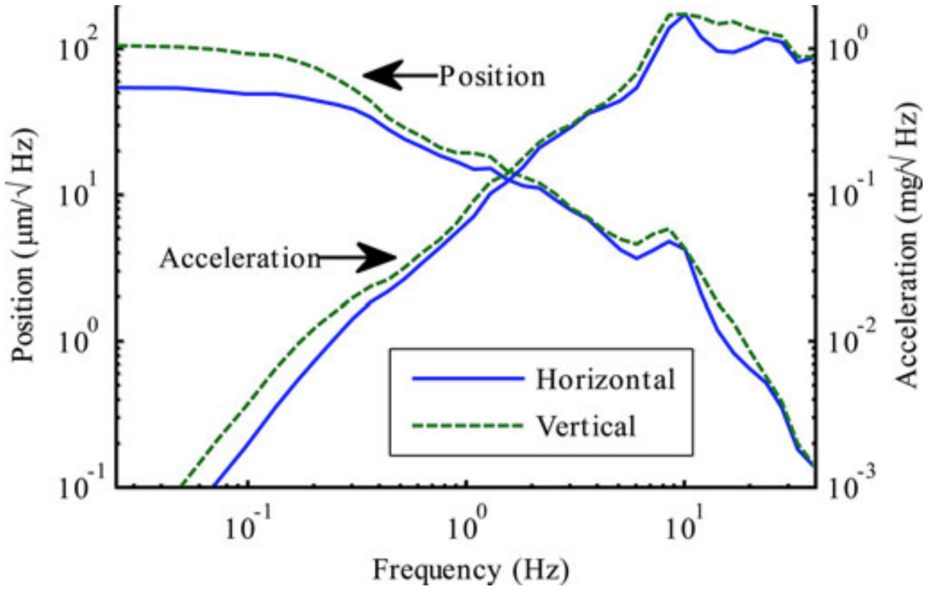

Figure 3.4: *Spectrum of position error and acceleration during "hold-still" task.*

3.4 Control Strategy

The main goal of the robot control strategy is the cancellation of hand tremor and erroneous movements, guaranteeing the tracking of the surgeons desired position.

Since Micron is a handheld tool, the design of the position control has to take in consideration the presence of the human in the loop. Reducing a human to a linear system and neglecting many details, the hand motion becomes a combination of the human desired position and the hand tremor: the first is considered as the reference position for the loop, while the hand tremor acts like a disturbance:

$$X = R_H + D_H \tag{3.1}$$

R_H: desired positon
D_H: disturbance

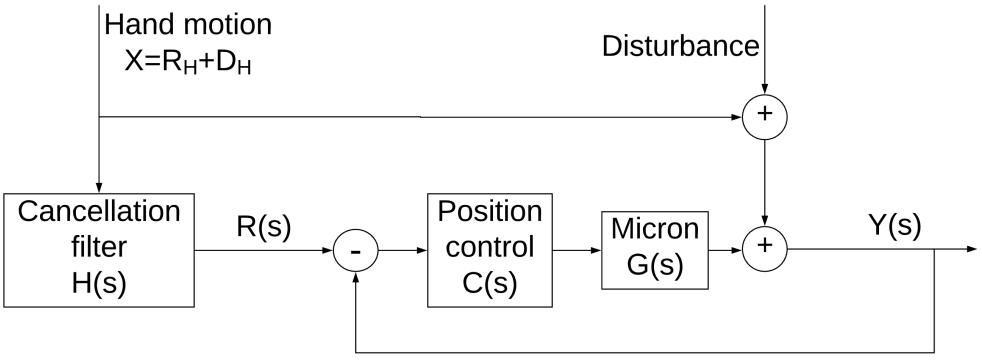

Figure 3.5: *Block diagram of the position control.*

Firstly, a cancellation filter $H(s)$ computes the estimation $R(s)$ of the human desired position, filtering the tremor.
The filter requirements accord with the nature of tremor and the dynamics of the human eye-hand coordination: $H(s)$ must have a unit gain at low frequency ($1Hz$) to guarantee the goal position and don't compromise the eye-hand coordination, and should have high attenuation at $10Hz$ to cancel tremor components. Hence, a shelving filter having a low corner frequency, a flat shelf ($1Hz$) and a high corner frequency ($10Hz$) [28], is used.

$$R(s) = H(s)(R_H + D_H) \tag{3.2}$$

Following, the $R(s)$ turns in the reference for the position loop. The position is controlled in link-length space using the inverse kinematics: the goal position and current position of the tool tip are converted by the inverse kinematics to link-lengths related to the six piezoelectric motors. A PID control $C(s)$ guarantees the tracking of the reference position $R(s)$. The feedback control is the current position of the end effector:

$$Y(s) = G(s)C(s)R(s) \tag{3.3}$$

If $H(s)$ recovered R_H perfectly and R_H was tracked perfectly by the position loop, then $Y(s) = R_H$ and the tremor would be completely cancelled. The actuators are updated 1000 times per second.

3.5 Poses and Coordinates

With the purpose of relating handle and end-effector position and orientation, in the system there are three main coordinates frames: manipulator coordinates (m), end-effector coordinates (e), world coordinates (w) and link-length space (l).

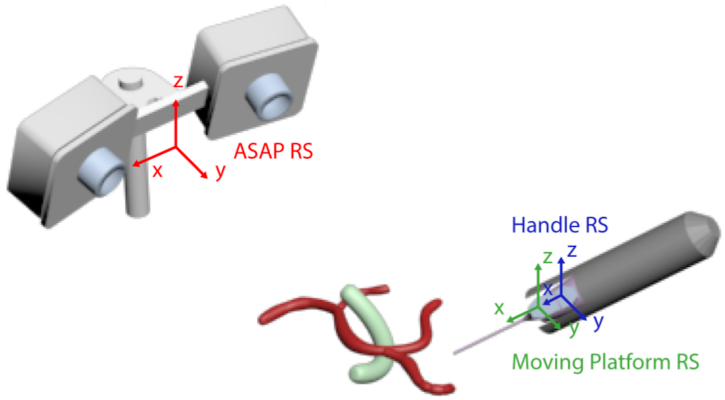

Figure 3.6: *Micron setup with reference systems.*

The world coordinates coincides with the ASAP ones. The ASAP measures the positions of the handle and the end effector LEDs, computing the manipulator pose P_m, the end-effector pose P_e, with respect to the world coordinates.

$$P_e = \begin{bmatrix} x_{x_e} & y_{x_e} & z_{x_e} & p_{x_e} \\ x_{y_e} & y_{y_e} & z_{y_e} & p_{y_e} \\ x_{z_e} & y_{z_e} & z_{z_e} & p_{z_e} \\ 0 & 0 & 0 & 1 \end{bmatrix} \qquad P_m = \begin{bmatrix} x_{x_m} & y_{x_m} & z_{x_m} & p_{x_m} \\ x_{y_m} & y_{y_m} & z_{y_m} & p_{y_m} \\ x_{z_m} & y_{z_m} & z_{z_m} & p_{z_m} \\ 0 & 0 & 0 & 1 \end{bmatrix} \tag{3.4}$$

$$X_w = P_m X_m \qquad X_w = P_e X_e \tag{3.5}$$

$$X_w = \begin{bmatrix} x_w \\ y_w \\ z_w \\ 1 \end{bmatrix} \qquad X_e = \begin{bmatrix} x_e \\ y_e \\ z_e \\ 1 \end{bmatrix} \qquad X_m = \begin{bmatrix} x_m \\ y_m \\ z_m \\ 1 \end{bmatrix} \tag{3.6}$$

Since the 6-DOF Micron is primarily controlled in link-length space, the positions are converted to six link-lengths by the inverse kinematics.

$$X_l = J(x)^{-1} X_w \tag{3.7}$$

The force signal is acquired in end-effector coordinates, then it is transformed in world coordinates to be related with the world position.

3.6 Onboard Force Sensor

The direct force feedback is accomplished using a 2-dof FBG force sensor designed and developed by the John Hopkins University [29]. In the following, basic knowledge of FBG sensors and restrict informations about the used sensor are treated.

3.6.1 Fiber Bragg Technology

An optical fiber is a cylindrical dielectric waveguide that transmits light with a very small amount of losses, exploiting the total internal reflection process. The fiber consists of a core surrounded by a cladding layer: having a greater cladding's refractive index than the core's one, the optical signal is confined in the core. To ensure more structural rigidity and strength, the fiber is covered by a buffer. According to the total internal reflection process, the light rays of light, that pass through the boundary of two different refractive index material, changes direction according to the Snell's law:

$$n_1 sin\theta_1 = n_2 sin\theta_2 \tag{3.8}$$

n =refractive index

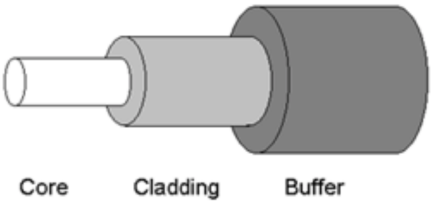

Figure 3.7: *Optic fiber structure.*

Passing from a greater n to a smaller n, a critical angle exists, such that:

$$\theta_1 = \theta_{cr} \qquad \theta_2 = 90deg \tag{3.9}$$

That angle can be computed by:

$$sin\theta_{cr} = \frac{n_2}{n_1} \tag{3.10}$$

Then, if

$$\theta_1 > \theta_{cr} \tag{3.11}$$

the total internal refraction happens. Hence, the light inside the optical

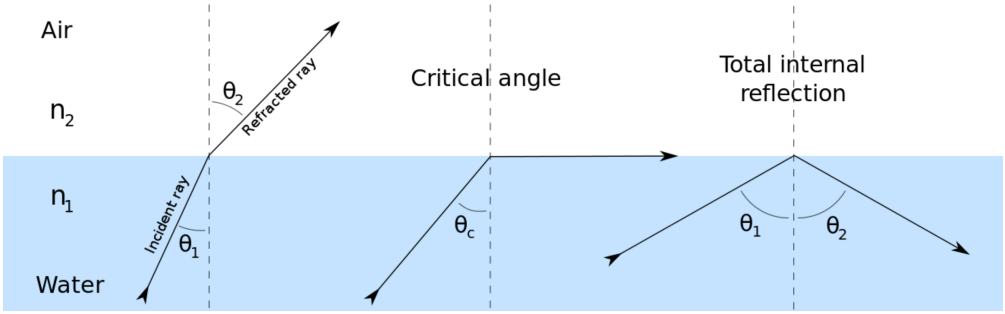

Figure 3.8: *Example of total internal refraction index between water and air.*

fiber must be transmitted with a refractive index greater to the critical one, so the light can be confined in the core and achieve the opposite side of the fiber.

The Fiber Bragg Grating is a modification of optical fiber's core in a precise area, that allows a proper modulation of the refraction index. The modified fiber's area acts like a filter: it selects particular wavelengths and reflect them backwards along the fiber. The main reflected wavelength is

called Bragg wavelength: it is just related to the pace of the Fiber Bragg Grating and to the effective refraction index.

$$\lambda_b = 2n_{eff}\Lambda \tag{3.12}$$

Λ = FBG pace
n_{eff} = Effective refraction index

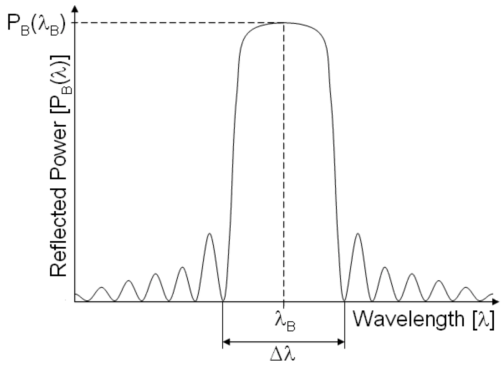

Figure 3.9: *Reflected Bragg wavelength.*

The pace of the FBG and the effective refraction index are linearly sensible to strain and temperature variation: for that reason the FBG could be used like strain and temperature sensor, exploiting his Bragg wavelength variation.

3.6.2 Micron's Embedded Force Sensor

The FBG sensor described in the folloing has been designed and built by the John Hopkins University (Baltimore, MD) [29].

The shaft of the sensor is a 50 mm long titanium wire with 0,5 mm diameter. Three optical fibers are embedded evenly along the surface of the wire, 120^o from one another. At the end of each fiber, there is a Fiber Bragg Rating (FBG). The FBG sensor used is OS1100, from Micron Optics, Inc. (Atlanta, GA), with a central wavelength of 1550 nm. The active fiber section of the sensor is about 10-mm long, starting 5mm from the tip of the fiber. The Bragg wavelength value is acquired through an Optical Sensing Interrogator (SM130-700): it allows static or dynamic real time acquisition, providing fast and accurate readings of several FBG sensors. The wavelength interrogator has a resolution of 0.001 nm and

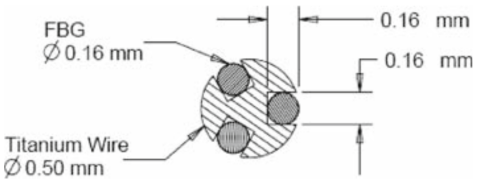

Figure 3.10: *Embedded force sensor structure*

scan frequency up to 2 kHz. The wavelength range is 1510-1590 nm. In our case, the force sensor is embedded with the end effector tool: a needle pass through the sensor shaft, allowing just the tip protrude for few millimeters.

3.6.3 Force Signal

The main issue for the proper operation of the admittance control is the data acquisition and interpretation. In the following section, the entire force signal acquisition and filtering procedure is investigated.

The sensitivity of the FBG sensor depends on the nature of the strain or load applied on the shaft the fibers are embedded within. In order to compute the lateral force components exerted on the lateral sensor shaft, it's useful to measure the related Bragg wavelengths variations of the three FBG sensors embedded in: they are strongly affected by lateral force and temperature variation, but also axial variation can slightly affect these measures. Hence, the variations of the Bragg wavelengths are proportional to strain and temperature:

$$\Delta\lambda = k_\epsilon \epsilon + k_T \Delta T \tag{3.13}$$

To get the lateral force components, It's possible to provide cancellation of the axial component and temperature effect. Assuming that there is not temperature variation along the surface of the shaft, the three FBG are subjected to the same and, under construction hypothesis, should be the same. Also, the axial force component, due to the really small shaft diameter, can be considered equal for all of them. Hence, subtracting the mean value of the three FBG from the each wavelength variation, it is possible to remove the common terme such as noises, axial strain and temperature effect:

$$\Delta S_i = \Delta\lambda_i - \Delta\lambda_{mean} = k_{\epsilon i}\epsilon_i - \frac{1}{3}\sum k_{\epsilon i}\epsilon_i \tag{3.14}$$

Finally, it has been proven that there is a linear relationship between ΔS and F: the following is the main equation that relates the lateral forces with the compensated variations of the Bragg wavelengths.

$$\begin{bmatrix} \Delta S_1 \\ \Delta S_2 \\ \Delta S_3 \end{bmatrix} = \begin{bmatrix} k_{x1} & k_{y1} \\ k_{x2} & k_{y2} \\ k_{x3} & k_{y3} \end{bmatrix} \begin{bmatrix} F_x \\ F_y \end{bmatrix} \tag{3.15}$$

Once the wavelengths have been acquisite and the temperature and strain compensation has been performed, the signal has to be filtered. The signal is still really noisy and not suitable to for the admittance control. The difference between signal rate acquisition (2kHz) and actuators update rate (1kHz) suggests to exploit an average value every two scans: in this way it's possible to get a less noisy final signal frequency at 1kHz. Using the Enlight software (Micron Optics Inc.) is possible to analyze the frequency spectrum of the signal. It has been deduced that the signal is affected by a noise with magnitude around 5dB, distributed all over the spectrum. A Moving Average filter has been used to reduce the noise in the interesting band, since it is optimal for reducing random noise while retaining a sharp step response: in spite of the moving average filter cannot separate one band of frequencies from another (poor performance in frequency domain), it is an exceptionally good smoothing filter (good performance in the time domain). A MA filter is a Finite Impulse Response whose weights are equal to $1/M$. It doesn't require feedback and it is inherently stable.

$$MA(t) = \frac{1}{M} \sum_{k=0}^{M-1} x(t-k) \tag{3.16}$$

A trade-off between the time response and the cut-off frequency has been required to compute the suitable length of the window M.
Finally, the choice fell on $M = 20$.

Looking at the transfer function of the moving average filter

$$H(z) = \frac{1 + z^{-1} + ... + z^{-(M-1)}}{M} \tag{3.17}$$

we note that the computational time for each value is not negligible. That's why a recursive implementation has been preferred to the standard one.

If

$$y_M(n) = \frac{1}{M} \sum_{k=0}^{M-1} x(n-k) \tag{3.18}$$

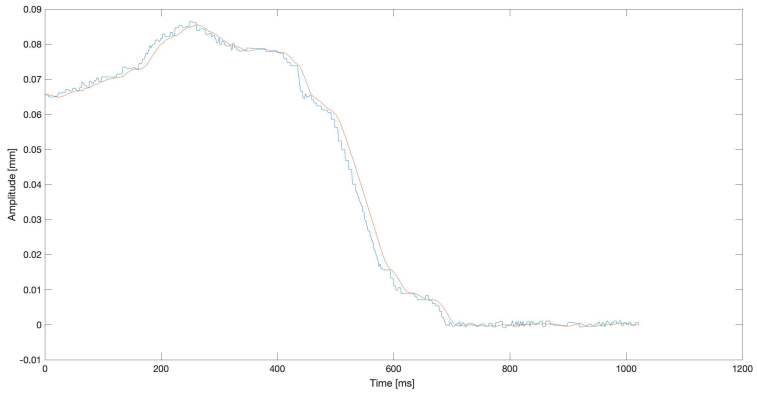

Figure 3.11: *An example of a FBG channel signal: the blue line reppresents the non filtered signal, the red while is the corresponding signal filtered by a recursive moving average filter with* $m = 20$*. The y-axis represents the wavelength in [mm], the x-axis the time in [ms]*

and

$$y_{M-1}(n-1) = \frac{1}{M-1} \sum_{k=1}^{M-1} x(n-k) \tag{3.19}$$

Then

$$\sum_{k=0}^{M-1} x(n-k) = x(n) + \sum_{k=1}^{M-1} x(n-k) \tag{3.20}$$

and

$$My_M(n) = x(n) + (M-1)y_{M-1}(n-1) \tag{3.21}$$

substituing $\lambda = \frac{M-1}{M}$

$$y_M(n) = \lambda y_{M-1}(n-1) + (1-\lambda)x(n) \tag{3.22}$$

If M is large

$$\lambda \simeq 1 \tag{3.23}$$

and

$$y_{M-1}(n) = y_M(n) \tag{3.24}$$

Then the final recursive equation for the filter is

$$y(n) = \lambda y(n-1) + (1-\lambda)x(n) \tag{3.25}$$

The bode plot [fig. 3.10] shows the pass band (below 30Hz) and the linear phase in the interesting band, that guarantees a constant delay: The step response [fig. 3.11] show that the system takes 0.1s to complete the transaction from two different values: that is important to guarantee a timely answer to force peaks.

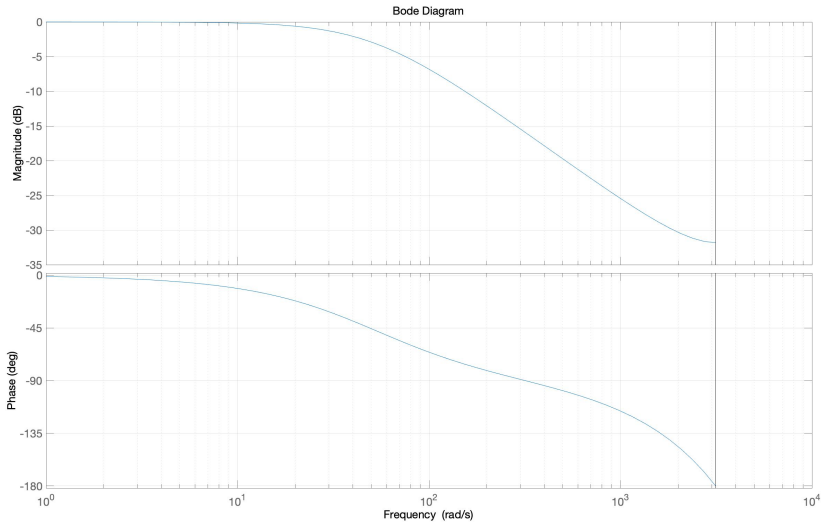

Figure 3.12: *Bode plot of the recursive moving average filter.*

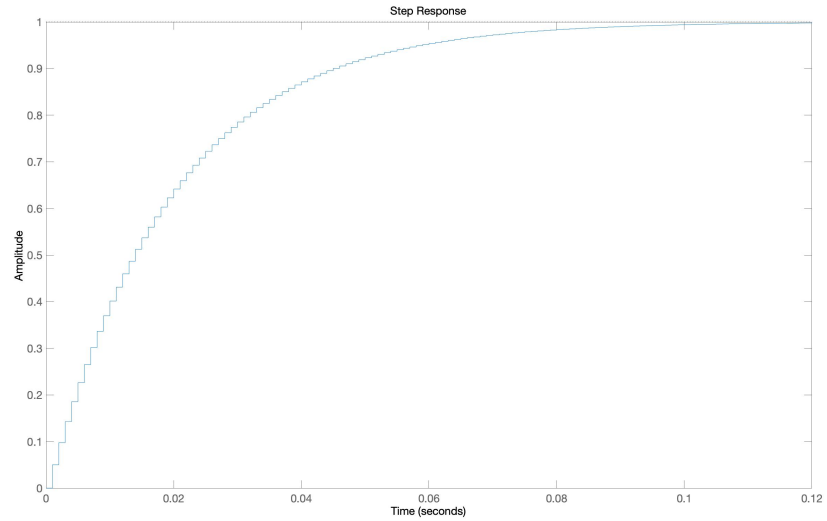

Figure 3.13: *Time response of the recursive moving average filter.*

3.6.4 Calibration

Once the Bragg wavelengths value have been acquired and filtered, they must be transformed by the linear equation (see before) in force signal in $[mN]$.

The calibration setup consists in applying a known weight ($1.97g$) on the tip of the sensor. Then, measuring the wavelength variation, since the relation between force and wavelength is linear, it has been possible to compute the calibration matrix.

$$\begin{bmatrix} \Delta S_1 \\ \Delta S_2 \\ \Delta S_3 \end{bmatrix} = \begin{bmatrix} k_{x1} & k_{y1} \\ k_{x2} & k_{y2} \\ k_{x3} & k_{y3} \end{bmatrix} \begin{bmatrix} F_x \\ F_y \end{bmatrix} \tag{3.26}$$

The force applied was:

$$F = F_x = F_y = 1.97[g] * 9.81[m/s^2] = 19.3[mN] \tag{3.27}$$

The linear system has been solved by decoupling the effects of F_x and F_y: rotating the sensor about its long axis and loading the sensor with the known weight, is possible to compute the calibration matrix. Four calibration sets were performed at 0, 90 degrees and 180, 270 to confirm. The force, then, can be calculated using the sensor readings and the pseudo-inverse of the calibration matrix:

$$F = K^{+}\Delta S \tag{3.28}$$

For this sensor the pseudo-inverse calibration matrix is:

$$K^{+} = \begin{bmatrix} -116.7993 & -734.4994 & 894.8806 \\ -1081.8758 & 360.7415 & 826.3118 \end{bmatrix} \tag{3.29}$$

From [22] we know that the sensor has a resolution of 0.25 mN.

3.7 Load Cell

The Fiber Bragg Grating force sensor has just two degrees of freedom: it can measure applied forces perpendicular to the end-effector. i.e. forces applied on the side of the shaft.

A load cell mounted underneath the workpiece has been used to achieve three degrees of freedom: the force measured by the load cell is the sum of the whole applied forces by the end-effector (perpendicular and parallel forces). Then, the load cell data and the onboard sensing data allow to compute the parallel applied force:

$$F_z = \sqrt{F_{loadcell}^2 - F_x^2 - F_y^2} \tag{3.30}$$

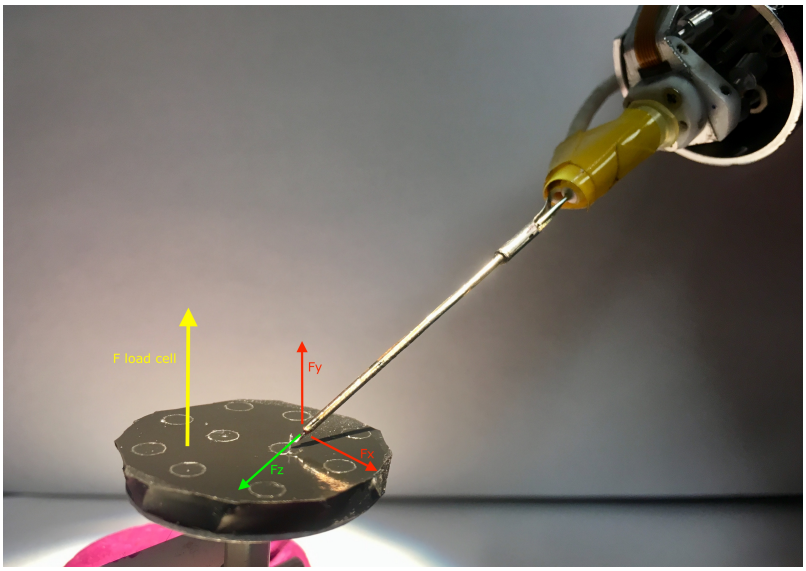

Figure 3.14: *The red forces are perpendicular to the end-effector and measured by the onboard sensor. The green force is parallel to the end-effector, it's computed by equation 3.1 .*

Chapter 4

Interaction Control Theory

4.1 Introduction

In this chapter the classic interaction control theory is explained: a manipulator with known dynamic model is used as example to show the admittance control's main concepts.

Control of interaction between a robot and the environment is important for successful execution of a task where the robot's end effector has to perform some operations in contact with unknown or known objects. During interaction, the environment constraints the end effector planned path and the use of a purely motion control strategy for controlling the trajectory could fail: in practice, the interaction between robot and environment may give rise to a contact force causing a deviation of the end effector from the desired trajectory. Since the control system reacts to reduce such deviation, contact force increases until actuators saturate. Only using accurate model of both kinematics and dynamics of the robot, geometry and mechanical features of the environment, it could lead to a successful execution. However, an accurate knowledge of the environment is difficult to obtain.
This drawback can be overcome if the interaction performs like a compliant behavior: interaction control strategy. The monitoring of the contact force is the main aim of the interaction control strategy: since the contact force describes the state of the interaction, the performance can be increased using a force/torque sensor.

4.2 Classification

There exist two main idea of interaction control strategy [17]:

- In *indirect force control*, the force control is achieved via motion control, without ensuring a force feedback loop: the position error is related to the contact force through impedance or mechanical stiffness.

- In *direct force control*, it's possible to achieve a desired force value, ensuring a force control loop closed around the inner motion control loop.

Stifness control and *impedance control* belong to the first category: the position error is related to the contact force through a mechanical stiffness or impedance.
If a detailed model of the environment is available, the *hybrid positon/force control*, second category, allows to control the positon along the unconstrained task directions and force along the constrained task directions.
When a detailed model of the environment is not available, a *parallel control* can be used: an outer force control loop dominates a inner position control loop, in order to ensure a force tracking along the constrained task directions.

In neurosurgery procedure, obviously it's really hard to modelize the environment due to a great diversity of tissues. Furthemore, surgeons don't need to track a force reference but need to avoid the force thresholds exceeding. To achieve these goals, an impedance control has been taken into consideration. In the following, both impedance and admittance control are treated.

4.3 Impedance and Admittance Control

In this section the theory of *impedance* and *admittance control* is explained. Due to task requirements and tool features only the forces have been considered, moments are neglected. Since the main tasks of manipulators are planned in end-effector coordinates, task space feedback is utilized: end-effector position is computed via the kinematics relationships from the joint measurements. *Dynamic model* of the manipulator, consisting of finding the relationship between the forces exerted by the robot and the joint position, is not obtained here. So, we consider the given dynamic

equation:

$$B(q)\ddot{q} + C(q,\ddot{q})\dot{q} + F\dot{q} + g(q) = \tau - J_x^T(q)f_e \tag{4.1}$$

q= joints variable
$B(q)$ = inertia matrix
$C(q,\dot{q})$ = vector of Coriolis and centrifugal torques
$g(q)$ = vector of gravity forces and torques
F = friction torques
J_x = Jacobian matrix
f_e = applied forces on end-effector
τ = joints forces

4.3.1 No Iteractions ($f_e = 0$)

To obtain and analyze the interaction control strategy, we use the *inverse dynamics control*: it is useful to linearize and to decouple the manipulator dynamics via feedback. Non linearities such $C(q,\dot{q})$, F and $g(q)$, being added to the control input, can be cancelled. Decoupling is achieved by weighting the control input by the inertia matrix $B(q)$.

Hence, having $f_e = 0$ (no interactions with the environment), the joint torque to achieve a desired position (q) can be chosen as:

$$\tau = B(q)\alpha + C(q,\dot{q})\dot{q} + F\dot{q} + g(q) \tag{4.2}$$

α is the new control input to be properly designed: it represents the required acceleration in joints space to achieve the desired end-effector task. Indeed, if we substitute the inverse dynamics control equation into the dynamics model, we get a linear and decoupled system:

$$\ddot{q} = \alpha \tag{4.3}$$

Then, we should move from joints space to task space. Having:

$$\dot{p}_e = J_x(q)\dot{q} \tag{4.4}$$

$$\ddot{p}_e = J_x(q)\ddot{q} + \dot{J}_x(q,\dot{q})\dot{q} \tag{4.5}$$

We obtain:

$$\alpha = J_x^{-1}(q)(a_x - \dot{J}_x(q,\dot{q})\dot{q}) \tag{4.6}$$

And then, substituting in the dynamics model:

$$\ddot{x}_d = a_x \tag{4.7}$$

a_x is the new control variable to be properly designed: it represents the required acceleration in task space to achieve the desired end-effector's task. For this purpose, a position error between the desired and current end effector position is defined by:

$$\Delta x_{de} = x_d - x_e \tag{4.8}$$

Hence we can choose:

$$a_x = \ddot{x}_d + D_x \dot{\Delta} x_{de} + K_x \Delta x_{de} \tag{4.9}$$

Finally substituting the control variable in the dynamic equation, we can get the close-loop dynamic behavior of the position error:

$$\Delta \ddot{x}_{de} + D_x \Delta \dot{x}_{de} + K_x \Delta x_{de} = 0 \tag{4.10}$$

The system is stable for any choice of D_x and K_x.

4.3.2 Iteractions ($f_e \neq 0$)

Then, it is useful to observe the behavior of an inverse dynamics control in presence of no null contact force $f_e \neq 0$.

It leads to:

$$\ddot{q} = \alpha - B^{-1}(q) J_x^T(q) f_e \tag{4.11}$$

$$\Delta \ddot{x}_{de} + D_x \Delta \dot{x}_{de} + K_x \Delta x_{de} = J_x(q) B^{-1}(q) J_x^T(q) f_e \tag{4.12}$$

This equation relates the force applied to the end effector to the position error through an active impedance: the presence of $J_x B^{-1} J_x^T$ makes the system coupled and nonlinear.
However, measuring the applied forces on the end effector, it is possible to keep linearity and decoupling during the interaction with the environment. Modifying the dynamics model:

$$\tau = B(q)\alpha + C(q, \dot{q})\dot{q} + F\dot{q} + g(q) + J_x^T(q) f_e \tag{4.13}$$

And using the following control strategy:

$$\alpha = J_x^{-1}(q) M^{-1} (M\ddot{x}_d + D\dot{\Delta} x + K\Delta x - M\dot{J}_x(q, \dot{q})\dot{q} - f_e) \tag{4.14}$$

$$a_x = \ddot{x}_d + M^{-1}(D_x \Delta \dot{x}_{de} + K_x \Delta x_{de} - f_e) \tag{4.15}$$

Hence the position error dynamics in task space is

$$M\ddot{\Delta x}_{de} + D\dot{\Delta x}_{de} + K\Delta x_{de} = f_e \tag{4.16}$$

This equation is linear and decoupled.
The interaction behavior is acting like a mass-damper-spring system: tuning M, D and K, it's possible to change the behavior of the end effector during contact forces.
This is called *impedance control*: the control strategy receives an input position and generates equivalent forces to achieve the desired position of the end-effector.

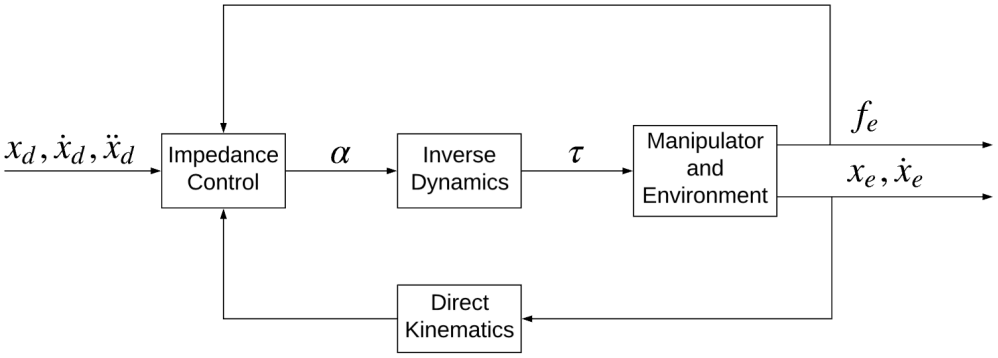

Figure 4.1: *Impedance control.*

4.3.3 Admittance Control

In impedance control ,the selection of good parameters that guarantee a satisfactory compliant behavior, could be inadeguate to achieve good tracking performance of the desired position trajectory when the end effector moves in free space being affected by disturbance. Since the dynamics model is often obtained by an identification procedure, the inverse dynamic control compensation could be inaccurate. This leads to:

$$\ddot{q} = \alpha - d_q \tag{4.17}$$

$$a_x = \ddot{x}_d - d_x \tag{4.18}$$

$$d_x = J(q)d_q \tag{4.19}$$

And then, under force interactions:

$$M\ddot{\Delta x}_{de} + D\dot{\Delta x}_{de} + K\Delta x_{de} = f_e + Md_x \tag{4.20}$$

A big issue is to achieve an effective disturbance rejection: at least at steady state, can be choose a low weight for the matrix $K^{-1}M$, which corresponds to a stiff control action with an equivalent light mass at the end effector. Such a feature can eventually conflict with the compliant behavior of the end effector interacting with a rather stiff environment.
A good solution is the separation of the impedance control from the motion control: so the desired position and contact forces are input to the impedance equation, which can compute a new desired position for the motion control.
Due to the change of output variable, this new control is called *admittance control*: given a force value, it returns a position value. Hence, the motion

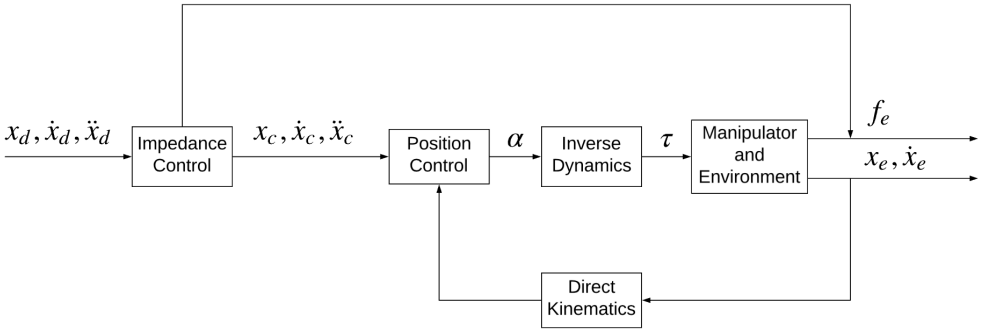

Figure 4.2: *Admittance control.*

parameters can be tuned to achieve a good disturbs rejection, while, the M, D and K can be tuned to achieve a desired behavior during contact forces. Necessarily, the motion control's bandwidth must be greater than the admittance control's one.

Chapter 5

Admittance Control

5.1 Introduction

In this section, the admittance control is implemented and customized to be used on Micron. A software based approach has been used: the control strategy has been implemented using LabView and during the normal operations the code is executed on a Real Time Machine build by*Micron Optics, Inc.*

5.2 Implemetation

The main goal of the admittance control is to modify the desired position of the end effector with the aim of reducing as much as possible the applied forces. For this purpose, the admittance control is placed before the position loop, so the set point of the position control is affected by the admittance control. The admittance control works satisfactorily and stably with the position loop: the motion's bandwidth is greater than force bandwidth. However, mass, stiffness and damping should be chosen reasonably to avoid instability in some cases.
Admittance controller is based on following inputs: virtual position, virtual velocity and external force, which affects the manipulator. It calculates desired position. When no forces act on manipulator and it reaches the desired position, there is no a force feedback. In this case, there is no constraints and the controller should fit the desired trajectory well. In case when the external force appears, the controller changes the position in relevance to stiffness and damping. In this way, it's possible to maintain position accuracy and meanwhile regulate applied forces.

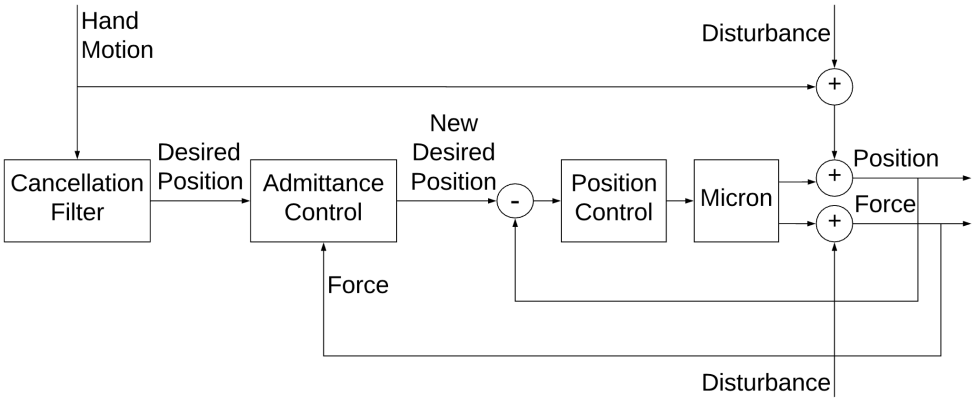

Figure 5.1: *Micron position and admittance block diagram.*

The implemented admittance control differs in some way form the classic admittance control:

- Since the end effector is a needle, two dimensions are negligible with respect the third, then the moment effects could be neglected. Moreover, accordingly with the tasks, the tool is designed to not require the moment control: in the following an admittance control dealing just with forces has been considered.

- In the admittance and position control loop, gravity compensation is not necessary due to the light weight of the end-effector: zeroing the sensor signal while the manipulator is being held in a task orientation is sufficiently to mitigate gravity force.

- Accordingly with the device, velocity of the end-effector is not directly measured, then it is not available in feedback. Therefore, it has been computed mathematically, deriving the position with respect the time in a discrete time domain.

$$\dot{P}_{goal} = \frac{d}{dt} P_{goal} \tag{5.1}$$

5.2.1 Input and output

The admittance filter receives as *input* the required position of the end effector and the force signal.

- The *desired position* of the end effector is 1x3 matrix:

$$P_{goal} = \begin{bmatrix} x_d & y_d & z_d \end{bmatrix} \tag{5.2}$$

The elements represent the position of the end effector in world (ASAP) coordinates.
Since the velocity is not directly measured from the robot, it is computed by deriving the desired position:

$$\dot{P}_{goal} = \begin{bmatrix} \dot{x}_d & \dot{y}_d & \dot{z}_d \end{bmatrix} \tag{5.3}$$

The derivative has been computed in discrete time domain.

- The *force signal* is acquired directly from the interrogator and, after the filtering procedure explained in the previous section, it achieve the admittance block. The f_z is acquired from the load cell and must be computed, see section 3.6 . It results:

$$F_e = \begin{bmatrix} f_x & f_y & f_z \end{bmatrix} \tag{5.4}$$

The previous force signal is defined in end effector coordinates.
Since the end effector position is in world coordinates, the force signal has to be transformed in world coordinates: the force vector has been multiplied by the end effector pose (rotational matrix). Starting from the end-effector pose, the rotational matrix is obtained:

$$R_e = \begin{bmatrix} r_{xx} & r_{xy} & r_{xz} \\ r_{yx} & r_{yy} & r_{yz} \\ r_{zx} & r_{zy} & r_{zz} \end{bmatrix} \tag{5.5}$$

Finally, it has resulted:

$$F_w = \begin{bmatrix} f_x & f_y & f_z \end{bmatrix} \tag{5.6}$$

The admittance control produces a new end effector desired position. Hence the *output* of the block is:

$$P_{admittance} = \begin{bmatrix} x_a & y_a & z_a \end{bmatrix} \tag{5.7}$$

5.2.2 Admittance block

As you can see in the previous section, having the forces measurement, the control strategy can be decoupled in the three world coordinates. Hence, three decoupled admittance controls relative to the three world coordinates

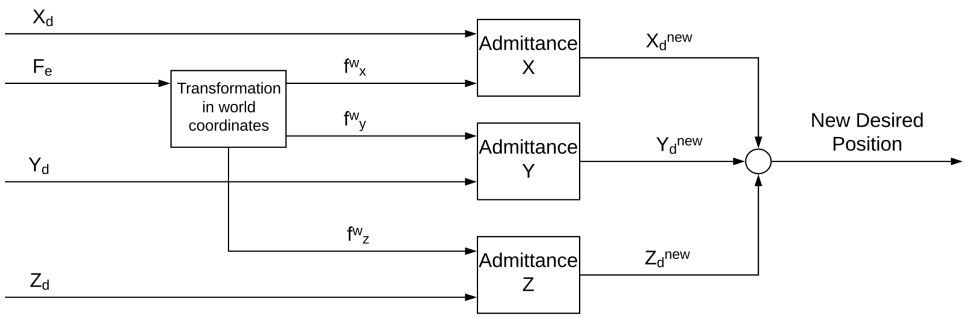

Figure 5.2: *Block diagram of the decoupled admittance control*

have been implemented.

Following the signal path as showed in the figure, the signal is acquired in end effector coordinates, after being transformed in world coordinates, has been decoupled and controlled by three different admittance block.

$$\begin{aligned} m_x\Delta\ddot{x} + d_x\Delta\dot{x} + k_x\Delta x &= f_x \\ m_x\Delta\ddot{y} + d_y\Delta\dot{y} + k_y\Delta y &= f_y \\ m_x\Delta\ddot{z} + d_z\Delta\dot{z} + k_z\Delta z &= f_z \end{aligned} \tag{5.8}$$

Where:

- $\Delta x = x_d - x_a$
  $\Delta y = y_d - y_a$ are the error position referred to the each direction.
  $\Delta z = z_d - z_a$

- m is the virtual inertia
- d is the virtual damper
- k is the virtual spring
- f is the force signal

To customize the control for different tasks, different parameters of the admittance control could be chosen for different directions. The new generated coordinates represents the new desired position the position control has to track.

Now on, just for simplicity, a single general equation is considered to explain the admittance block implementation. Starting from the basic impedance equation,

$$m\Delta\ddot{x} + d\Delta\dot{x} + k\Delta x = f \tag{5.9}$$

$$m(\ddot{x}_d - \ddot{x_a}) + d(\dot{x}_d - \dot{x}_a) + k(x_d - x_a) = f \tag{5.10}$$

it's possible to obtain the new velocity:

$$\ddot{x}_a = \frac{m\ddot{x}_d + d\dot{x}_d - d\dot{x}_a + kx_d - kx_a - f}{m} \tag{5.11}$$

The x_a is computed by integrating in a discrete time domain the $\ddot{x}_a$.

$$x_a = \int \dot{x}_a = \int\int \ddot{x}_a \tag{5.12}$$

The equation is implemented in the block diagram in figure.

Microneurosurgical tasks generally involve small velocities and very small accelerations. Considering the virtual mass-damper-spring system, the mass multiplies the value of the acceleration. Then, virtual mass coefficient has been set to zero and directly the new velocity has been computed: just a virtual damper and virtual spring are implemented.

$$\dot{x}_a = \frac{d\dot{x}_d + kx_d - kx_a - f}{d} \tag{5.13}$$

and

$$x_a = \int \dot{x}_a \tag{5.14}$$

5.2.3 Issues

There are some problems that afflict the implementation:

- The admittance control has no activation logic, an error position is generated according to the damper-spring dynamics every time a force sample is detected. Owing to noise and high sensibility of the force sensor, an error position is always present, producing annoying vibration.
- Since the applied force is not limited, the new position generated is not limited as well, that could make the actuators saturated. Anyway a big displacement could make difficult to perform the task, losing the coordination hand-manipulator.

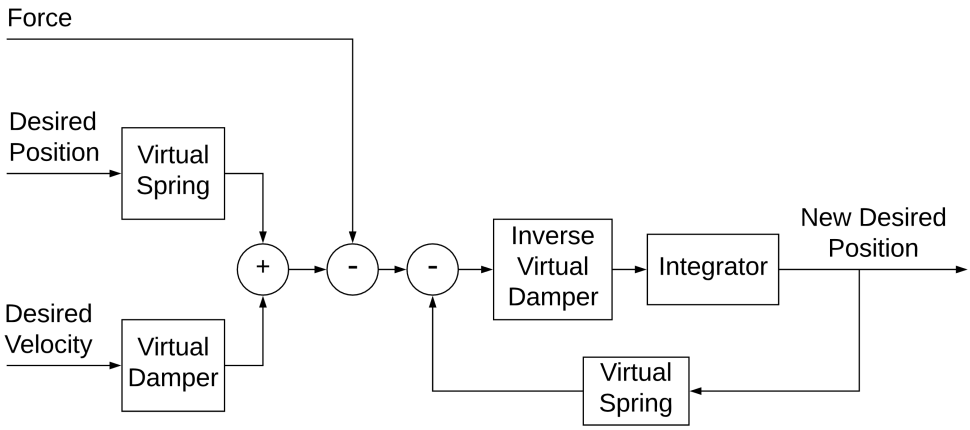

Figure 5.3: *Implementation of the admittance control, setting* $m = 0$

Force threshold

The aim is to avoid that the admittance dynamic actives whenever there is a small variation of the force signal, often it is due to noise oscillation. To restrict that occurrence it's helpful to set a force threshold, below which the force doesn't activate. Hence, a small change in the admittance system has been made:

$$m\ddot{x} + d\dot{x} + kx = |f - f_{threshold}|_0^\infty \tag{5.15}$$

An activation logic has been implemented with the aim of restrict the force signal between the force threshold and infinity. In such a way, small disturbance of the signal can be ignored.

Position limiting

A logic behavior has been implemented so that the new computed position cannot be more far than $2cm$ from the original trajectory. To do that, the new position is limited between:

$$x_a \in [x_d + 2cm, x_d - 2cm] \tag{5.16}$$

Furthermore, a logic behavior has been implemented as well with the aim of avoiding the reaching of the saturation threshold: when the motors are close to the saturation limit, the new position get a new range of motion:

$$\begin{aligned} x_a &\in [x_d + 2cm, x_d - lim_{sat}] \\ x_a &\in [x_d + lim_{sat}, x_d - 2cm] \end{aligned} \tag{5.17}$$

5.3 Tuning

The implemented admittance control has to be tuned. Since the admittance control is decoupled along the three world coordinates, it is possible to set different parameters along each direction. Anyway, for our purpose the three directions have been tuned in same way.

In the main admittance equation:

$$m\Delta\ddot{x} + d\Delta\dot{x} + k\Delta x = f \tag{5.18}$$

three different parameters have to be tuned: m, d, k.

As said before, since microneurosurgical tasks generally involve small velocities and very small accelerations, the *virtual mass* coefficient has been set to zero. Then, just the virtual damper and the spring have to be tuned.

The *virtual spring* can be interpreted as the stiffness value of the end effector: the stiffness is a measure of the resistance offered by an elastic body to deformation.
It guarantees a position error proportional to the force: higher the virtual spring's value, lower the position error generated.

$$\Delta x = \frac{f}{k} \tag{5.19}$$

Then, being Micron in contact with real easly damageable materials, accordingly to the test procedure and to the Soborthane features, the virtual spring has been set to $k = 0.02mN/m$.
Just in case different tissues or task are involved, setting a higher k, it is possble to have a more stiff instrument. The other way around, a lower k, allows to interacts with really sensitive tissues.

There are some disadvantages in having a low virtual spring. First of all, a low virtual spring causes a less position accuracy, since position error oscillations and noise are amplified. Furthemore, having a flexible instrument leads to a difficult hand-tool coordination.

The *virtual damper* guarantees a damping behavior of the system. Damping is an influence on the system that reduces, restricts or prevents the oscillations: it makes the derivative of the error position proportional

to the force.

$$\Delta \dot{x} = \frac{f}{d} \tag{5.20}$$

Higher is the virtual damping, smoother is the error position but slower the response, turning in a positon delay.

To evaluate the damping coefficient, a test has been carried on.
Micron was clamped in place and the end effector of the manipulator fixed in Sorbothane rubber: zeroing the sensor, any displacements would result in measured force. Position noise was eliminated by clamping the handpiece, thus removing the human-in-the-loop. Then, a digital offset of $20mN$ summed to a step stimulus of $10mN$ was injected in the force measurement.
Analyzing the control variable response (position error), related to the step force stimulus, it's possible to evaluate the tuning parameters: in Fig. 5.4 the position error response is plotted for many virtual damper values. Finally, a trade off between small oscillations and delay has been choosen and the virtual damper coefficient has been set to $d = 10$.

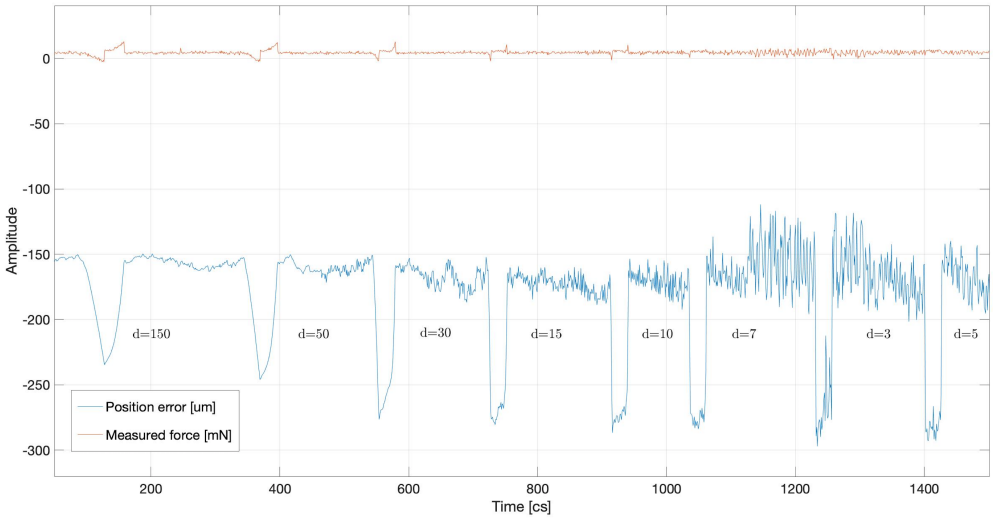

Figure 5.4: *The force step response results. Blue line represents the position error. Red line represents the measured force. Accordingly to different virtual damping values, the position error has different response.*

The damper effect is important to compensate the oscillations created by the virtual spring: lower is the virtual spring's coefficient, higher should be the virtual damper's coefficient.
The time response and the following delay is the main problem in damping

behavior.

Finally, the final set of parameters is:

$$\begin{aligned} m &= 0 \\ k &= 0.02 \\ d &= 10 \end{aligned} \tag{5.21}$$

5.4 Analysis

A response test has been used to analyzed the frequency response of the admittance control: the purpose of the following test is to obtain the frequency working bandwidth of the admittance control so as to compare it with typical operating frequency range in surgery.

To test the response properties of the admittance control system without the human in the loop, Micron was clamped in place, and the tip of the manipulator fixed in Sorbothane rubber, such that any displacement would result in a measured force.
The sensor was then zeroed, and a sinusoidal position stimulus (goal positon of the Micron position loop) was injected at frequencies ranging from $0.1Hz$ to $20Hz$. Position noise was eliminated by clamping the handpiece, thus removing the human-in-the-loop component. Position output was recorded by ASAP while injecting the stimulus. With the end-effector fixed, the force is directly influenced by displacement.

The system response transfer function was determined by comparing the positon measurement under admittance control with the direct stimulus input.
The resulting gain and phase Bode diagram have been obatined. The system was determined to have a maximum attenuation of $20dB$. The cutoff frequency occurs at $8Hz$ and corresponds to a sharp decrease in phase to -180^o at frequencies above the crossing.

Since motion during microsurgical procedures tends to be slow, movement generally occurs at frequencies less than $2Hz$ [23], which corresponds to a maximum attenuation of $10dB$. This is sufficient for limiting forces during microsurgical procedures and our peeling trials.

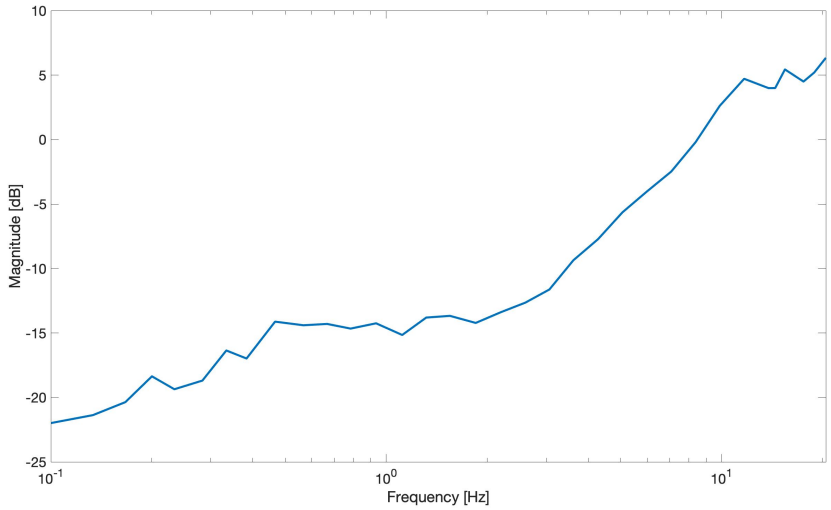

Figure 5.5: *Bode magnitude plot of the system response.*

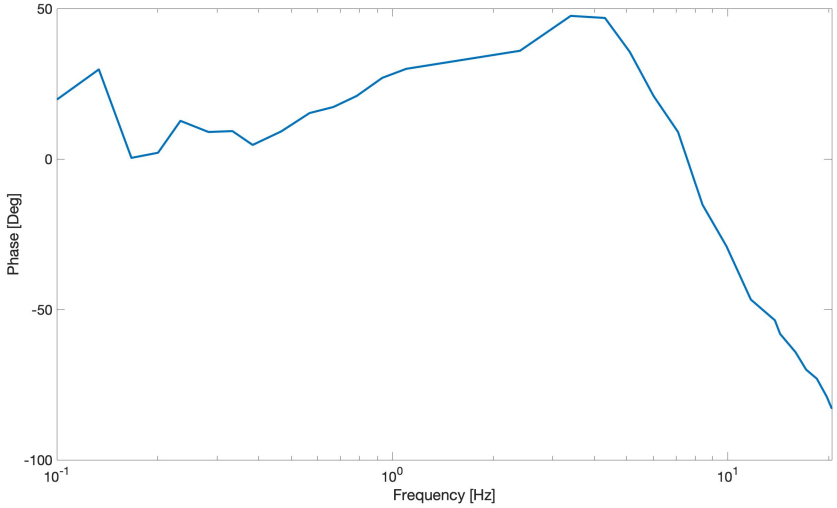

Figure 5.6: *Bode phase plot of the system response.*

Chapter 6

Test

6.1 Introduction

In this chapter, with the aim of validating the performance of the admittance control system, a repeatable test with human in the loop, under a board-approved protocol is introduced.

The experiment consists in a blunt dissection: it concerns a separation of tissues along tissue planes, through the use of blunt instruments. Blunt dissection takes a large proportion of time and requires great skill, can be tedious, nerve-wracking and risky.

Since the interaction with a real brain was not possible, an artificial set-up has been made in order to simulate the surgical environment and task. The experimental subject, not a surgeon, had considerable experience with Micron.

6.2 Experiment

The set-up is composed by:

- Sorbothane rubber ($2.5cm$ in diameter, $0.4cm$ of thickness) was chosen as an underlying substrate due to its tissue-like properties [24].
- 10 circles of polyethylene film were placed on each rubber workpiece, to enable a simulation of blunt dissection, ($12.7m$ thick, $3.6mm$ in diameter). To guarantee a certain fixing between the two parts, $24h$ has to been waited.

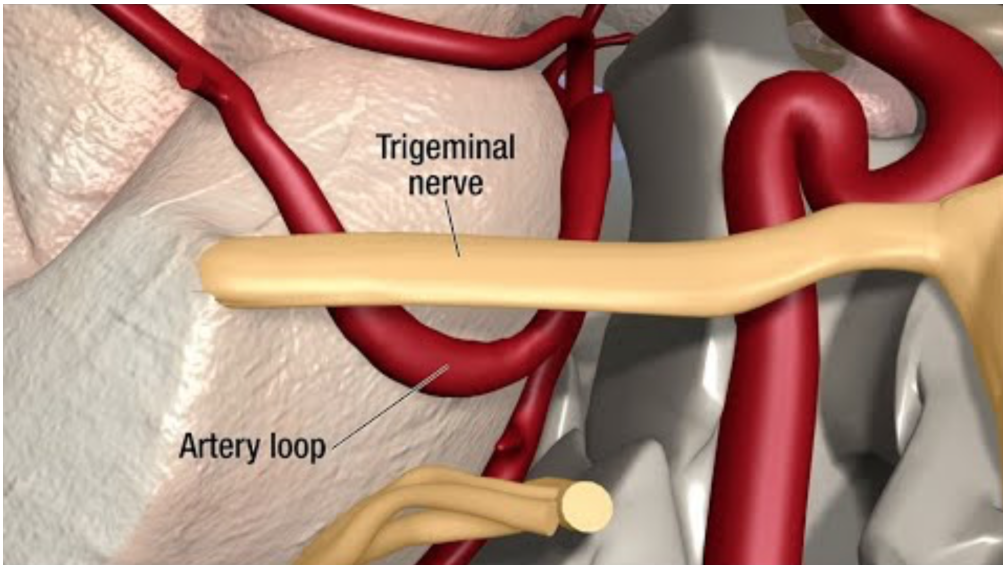

Figure 6.1: *Typical blunt dissection procedure: the trigeminal nerve has to be separated from the artery, applying small forces.*

The task involved the polyethylene peeling from the Sorbothane, using Micron. The procedure was performed under 16x magnification using a Zeiss OPMI 1 stereo operating microscope. Accordingly with surgeons procedure, the task has to be performed with constant velocity, at 1 or $2mm/s$, while holding the tool at 45^o-60^o with respect to the surface. In such a way, it is possible to limits the applied forces.
Due to the complexity of the procedure, the subject trained for several days before performing the test: the target consists in applying the least possible force in all the directions, trying to achieve a range of forces close to the ones achieved by surgeons.
In this particolar test, surgeons exert forces within $[5mN, 15mN]$. The subject results are significantly close to the surgeon's ones.

The forces in the three direction were measured in end-effector coordinates: to emulate a force sensor with three degrees of freedom, the sensor was augmented with a load cell mounted underneath the workpiece; load cell data were fused with the onboard sensing to obtain the force parallel to the long axis of the instrument.

A test consists in 2 rubber workpieces on which 8 circle films are attached (+2 films used in case a test failed due to unexpected events). The subject peels 8 circles under each of two test conditions: with position

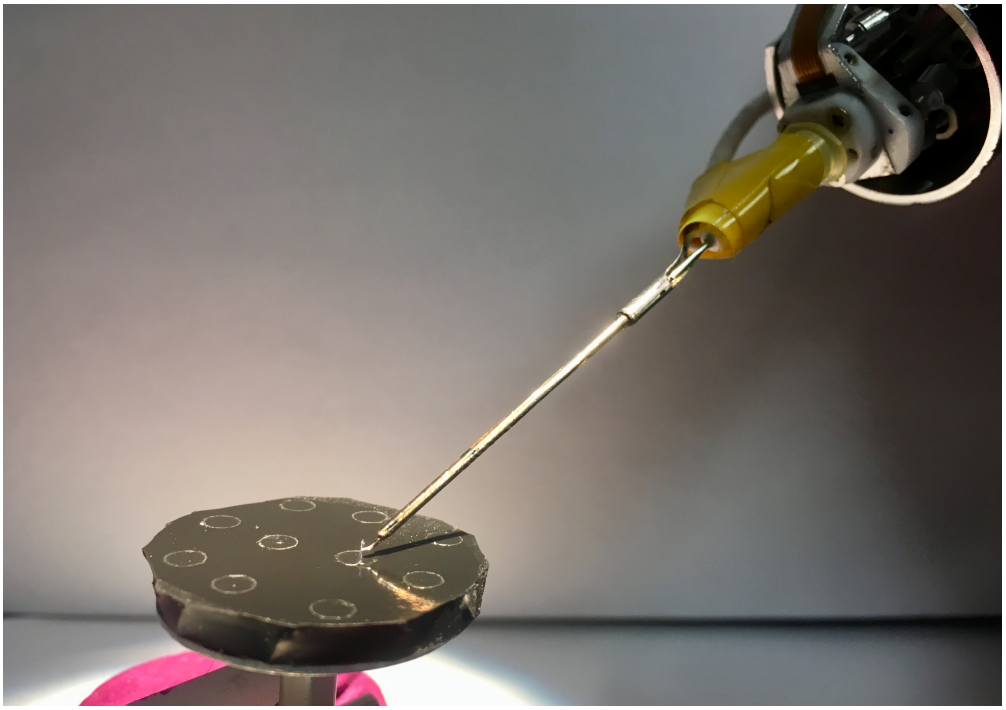

Figure 6.2: *Test setup and execution: Micron's end effector is peeling a circle film from the rubber.*

control only, and with position control joined with admittance control. Force was measured in three dimensions throughout each task.

6.3 Results

The forces exerted on brain tissue during neurosurgery procedure are really low and varied depending on the anatomical structure being manipulated and the maneuver performed.
The purpose of this work is to improve and simplify as much as possible the blunt dissection procedure, helping the surgeons in the force thresholding.

To evaluate the admittance control 4 tests have been performed. Hence, 64 trials have been peeled: 32 using position control, 32 using position control joined with admittance control.

The position control's parameters were set equal for both cases. While the admittance control was set with:

$$\begin{aligned} m &= 0mN/(m/s^2) \\ d &= 10mN/(m/s) \\ k &= 0.02mN/m \end{aligned} \tag{6.1}$$

The force data have been examined under position control and under admittance/position control. In the following graphs, together, the maximum and average force values, with standard deviation are presented.

In conclusion, during the test procedure, the results show that the use of an admittance control reduces the applied forces:

- the maximum exerted forces along x, y and z directions are respectively improved by 27%, 31% and 35%.
- the average exerted forces along x, y and z directions are respectively improved by 23%, 33% and 30%.

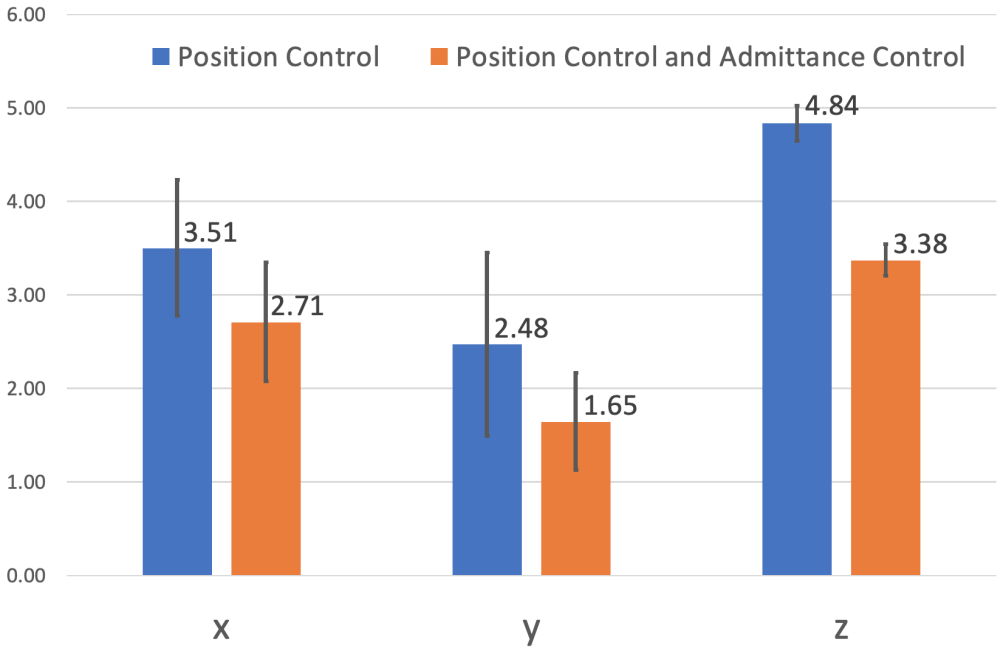

Figure 6.3: *In the graph, the mean applied forces in* $[mN]$ *during the tests is shown: it represents the average value of all the mean forces exerted during each test. The error bars represent the standard deviations of each direction. The blue columns represent the positon control data, while the orange columns represent the admittance/position control data.*

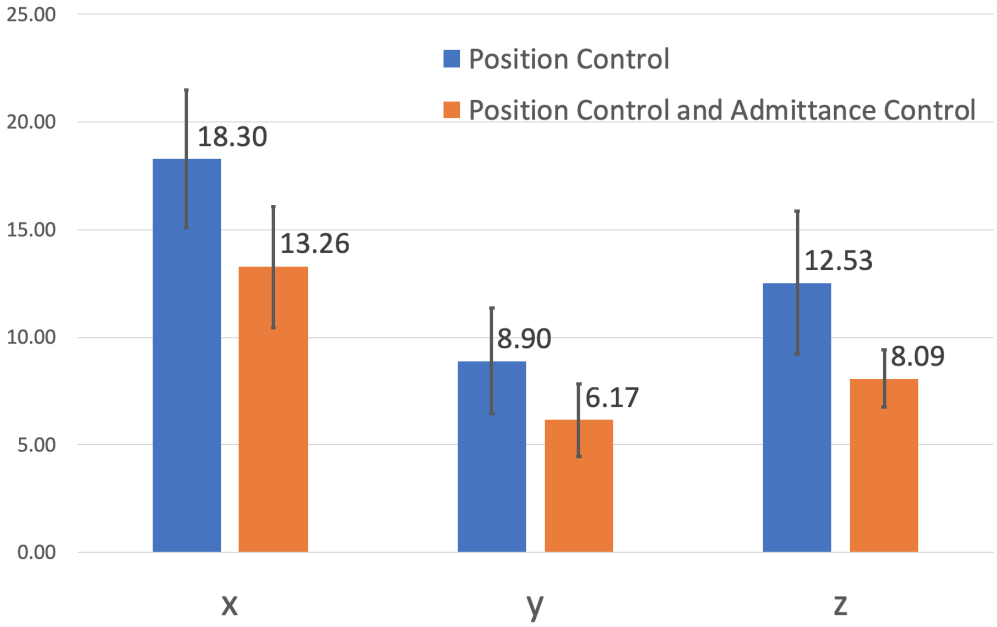

Figure 6.4: *In the graph, the maximum applied forces in* $[mN]$ *during the tests is shown: it represents the average value of all the maximum forces exerted during each test. The error bars represent the standard deviations of each direction. The blue columns represent the positon control data, while the orange columns represent the admittance/position control data.*

Chapter 7

Conclusion

This work reported on the implementation of admittance control to minimize force applied during blunt dissection with an active handheld microsurgical instrument, called Micron.
Using a FBG sensor, it is possible to measure small applied forces with a resolution of $0.25mN$. A classic admittance control exploits the force feedback to generate an error position accordingly with a virtual mass-damper-spring system.

Preliminary results showed a decrease in the maximum exerted force by 27% and 31% in the transverse coordinates, and 35% along the long axis of the instrument. A more trustable testing precedure with the help of expert surgeon has begun: Dr. Joseph N. Martel, *Department of Ophthalmology in University of Pittsburgh* (Pittsburgh, USA), is becoming familiar with the technology: an initial test showed a decrease in the maximum exerted force by 15% and 10% in the transverse coordinates, and 23% along the long axis of the instrument.
In the next tests, the surgeon is asked to help in the prameters tuning, so as to meet the needs of the surgeons and the stability of the tool.

Future work will deal with optimization of the control system tuning, and testing in under more realistic conditions.
The final objective consists on expanding the vessel avoidance approach, connecting the admittance control (designed in this thesis) togheter with a vessel segmentation from microscopy images, based on nerual networks [30], as to implement robust forbidden region virtual fixture Micron control.

Bibliography

[1] P. J. Kelly, "Stereotactic surgery: What is past is prologue," *Neurosurgery*, 2000.

[2] A. Morita, S. Sora, M. Mitsuishi, S. Warisawa, K. Suruman, D. Asai, J. Arata, S. Baba, H. Takahashi, and R. Mochizuki, "Microsurgical robotic system for the deep surgical field: development of a prototype and feasibility studies in animal and cadaveric models," *Journal of Neurosurgery*, 2005.

[3] S. M. Michalak, J. D. Rolston, and M. T. Lawton, "Incidence and predictors of complications and mortality in cerebrovascular surgery: National trends from 2007 to 2012," *Neurosurgery*, 2016.

[4] J. D. Lawrence, A. M. Frederickson, Y.-F. Chang, P. M. Weiss, P. C. Gerszten, and R. F. S. Jr, "An investigation into quality of life improvement in patients undergoing microvascular decom- pression for hemifacial spasm," *Journal of Neurosurgery*, 2017.

[5] M. L. DiLuna and K. R. Bulsara, "Surgery for petroclival meningiomas: a comprehensive review of outcomes in the skull base surgery era," *Skull Base*, 2010.

[6] S. M. Michalak, J. D. Rolston, and M. T. Lawton, "Incidence and predictors of complications and mortality in cerebrovascular surgery: National trends from 2007 to 2012," *Neurosurgery*, 2016.

[7] Kwoh, Hou, Jonckheere, and S. Hayati, "A robot with improved absolute positioning accuracy for ct guided stereotactic brain surgery.," *IEEE Transactions on Biomedical Engineering*, 1988.

[8] J. M. Drake, M. Joy, A. Goldenberg, and D. Kreindler, "Computer and robot-assisted resection of thalamic astrocytomas in children," *Neurosurgery*, 1991.

[9] A. Benabid, P. Cinquin, S. Lavalle, J. L. Bas, J. Demongeot, and J. D. Rougemont, "Computer-driven robot for stereotactic surgery connected to ct scan and magnetic resonance imaging.," *Stereotactic and Functional Neurosurgery*, 1987.

[10] A. Benabid, D. Hoffmann, S. Lavallee, P. Cinquin, J. Demongeot, J. L. Bas, and F. Danel, "Is there any future for robots in neurosurgery?," *Advances and Technical Standards in Neurosurgery*, 1991.

[11] A. Benabid, S. Lavallee, D. Hoffmann, P. Cinquin, J. Demongeot, and F. Danel, "Potential use of robots in endoscopic neurosurgery.," *Minimally Invasive Neurosurgery*, 1992.

[12] D. Glauser, H. Fankhauser, M. Epitaux, J.-L. Hefti, and A. Jaccottet, "Neurosurgical robot minerva: first results and current developments.," *Journal of Image Guided Surgery*, 1995.

[13] A. Benabid, D. Hoffman, A. Ashraff, A. Koudsie, and J. L. Bas, "Robotic guidance in advanced imaging environments," *Advanced Neurosurgical Navigation.*, 1999.

[14] Q. H. Li, L. Zamorano, A. Pandya, R. Perez, J. Gong, and F. Diaz., "The application accuracy of the neuromate robot - a quantitative comparison with frameless and frame-based surgical localization systems.," *Computer Aided Surgery*, 2002.

[15] G. Dogangil, B. Davies, , and F. R. y Baena, "A review of medical robotics for minimally invasive soft tissue surgery.," *Proceedings of the Institution of Mechanical Engineers, Part H: Journal of Engineering in Medicine*, 2010.

[16] B. C. Becker, S. Voros, L. A. Lobes, J. T. Handa, G. D. Hager, , and C. N. Riviere, "Retinal vessel cannulation with an image-guided handheld robot.," *Engineering in Medicine and Biology Society (EMBC), 2010 Annual International Conference of the IEEE*, 2010.

[17] J. W. Motkoski and G. R. Sutherland, "Why robots entered neurosurgery.," *Experimental Neurosurgery in Animal Models*, 2016.

[18] W. T. Ang, C. N. Riviere, and P. K. Khosla, "Design and implementation of active error canceling in handheld microsurgical instrument.," *Intelligent Robots and Systems*, 2001.

[19] B. Gonenc, M. A. Balicki, J. Handa, P. Gehlbach, C. N. R. andRussell H Taylor, and I. Iordachita, "Preliminary evaluation of a micro-force sensing handheld robot for vitreoretinal surgery.," *Intelligent Robots and Systems*, 2012.

[20] C. Yang, Y. Xie, S. Liu, and D. Sun, "Force modeling, identification, and feedback control of robot-assisted needle insertion: A survey of the literature," *Sensors*, 2018.

[21] B. Siciliano and L. Villani, *Robot Force Control*. Kluwer Academic Publishers, 1999.

[22] T. Haidegger, B. Benyo, L. Kovacs, and Z. Benyo, "Force sensing and force control for surgical robots," *Symposium on Modelling and Control in Biomedical Systems*, 2009.

[23] A. Q. Keemink, H. van der Kooij, and A. H. Stienen, "Admittance control for physical human robot interaction," *The International Journal of Robotics Research*, 2018.

[24] C. J. Payne, K.-W. Kwok, and G.-Z. Yang, "An ungrounded hand-held surgical device incorporating active constraints with force-feedback," *International Conference on Intelligent Robots and Systems*, 2013.

[25] W. T. Latt, R. C. Newton, M. Visentini-Scarzanella, C. J. Payne, D. P. Noonan, and J. Shang, "ôŔřŞheld instrument to maintain steady tissue contact during probe-based confocal laser," *IEEE Trans. Biomed. Eng.*, 2011.

[26] T. S. Wells, S. Yang, R. A. MacLachlan, L. A. L. Jr, J. N. Martel, and C. N. Riviere, "Hybrid position/force control of an active handheld micromanipulator for membrane peeling," *the international journal of medical robotics and computer assisted surgery*, 2015.

[27] R. A. MacLachlan and C. N. Riviere, "High-speed microscale optical tracking using digital frequency-domain multiplexing," *IEEE Trans. Instrum. Meas.*, 2009.

[28] MacLachlan, Becker, and C. Tabares, "Micron: an actively stabilized handheld tool for microsurgery.," *IEEE Transactions on Robotics and Automation*, 2012.

[29] M. Balicki, J. U. Kang, S. J. Phee, J. H. J. U. Kang, S. J. Phee, J. Handa, P. Gehlbach, and R. Taylor, "A sub-millimetric, 0.25 mn

resolution fully integrated fiber-optic force-sensing tool for retinal microsurgery," *International Journal of Computer Assisted Radiology and Surgery*, 2009.

[30] S. Moccia, S. Foti, A. Routray, F. Prudente, A. Perin, R. F. Sekula, L. S. Mattos, J. R. Balzer, W. F. Mayle, E. D. Momi, and C. N. Riviere, "Toward improving safety in neurosurgery with an active handheld instrument," *Annals of Biomedical Engineering*, 2017.